Article:
Morino, C., Conway, S., Philippe, M. et al. (7 more authors) (2023) Permafrost molards as an analogue for ejecta-ice interactions at Hale Crater, Mars. Icarus, 391. 115363. ISSN 0019-1035

https://doi.org/10.1016/j.icarus.2022.115363

Icarus 391 (2023) 115363

Contents lists available at ScienceDirect

Icarus

journal homepage: www.elsevier.com/locate/icarus

Permafrost molards as an analogue for ejecta-ice interactions at Hale Crater, Mars

Costanza Morino [a,*], Susan Conway [b], Meven Philippe [b], Coralie Peignaux [b], Kristian Svennevig [c], Antoine Lucas [d], Axel Noblet [b], Gioachino Roberti [e], Frances Butcher [f], Jake Collins-May [g]

[a] Université Savoie Mont Blanc, CNRS UMR 5204, Laboratoire Environnements, Dynamiques et Territoires de la Montagne, France
[b] Nantes Université, Université d'Angers, Le Mans Université, CNRS UMR 6112, Laboratoire de Planétologie et Géosciences, France
[c] Geological Survey of Denmark and Greenland, Denmark
[d] Université de Paris, Institut de physique du globe de Paris, CNRS, France
[e] Minerva Intelligence Inc., Canada
[f] The University of Sheffield, Department of Geography, UK
[g] The School of Geography, Politics and Sociology, Newcastle University, UK

ARTICLE INFO

Keywords:
Molards
Ejecta flows
Ground-ice
Permafrost
Volatiles

ABSTRACT

When the Hale impact crater penetrated the martian cryosphere 1Ga, landforms indicating post-impact volatile mobilisation were generated. We have found landforms in the ejecta blanket of Hale Crater similar to 'permafrost molards' found in periglacial environments on Earth, and probably related to the past or present presence of volatiles at/near the surface. Permafrost molards are conical mounds of debris associated with landslide deposits, resulting from the degradation of blocks of ice-rich material mobilised by a landslide in periglacial terrains. Here we analyse the spatial and topographic distribution of conical mounds around the Hale crater at regional and local scales, and compare them to those of molards on the deposits of the Mount Meager debris avalanche in Canada. Hale Crater's conical mounds are located at the distal boundary of the thickest ejecta blanket, which is the closest to the main crater. We observe a similar spatial arrangement of molards along the distal parts of the terminal lobe of the Mount Meager debris avalanche. We then compare the morphology and morphometrics of the conical mounds on Hale Crater to those of terrestrial molards on the Paatuut and Niiortuut rock avalanches in western Greenland. We find that morphology and setting of conical mounds within Hale Crater ejecta are consistent with the formation pathway of molards on Earth. We infer that they originated from blocks of ice-cemented regolith that were produced by the Hale-crater-forming impact, transported by the ejecta flows, and finally degraded to cones of debris (molards) on loss of the interstitial ice. The similarities in distribution between the ejecta flows of Hale and Mount Meager debris avalanche on Earth suggest that the mounds resulted from the rheological separation of the ejecta flows, with a relatively fluid-poor phase that allowed the volatile-rich blocks to survive transport. This supports the prevailing hypothesis that the Hale impact event penetrated the martian cryosphere, providing important constraints on the rheology of martian ejecta deposits.

1. Introduction

Ground ice is common at mid to high latitudes on Mars (Carr, 2007; Schorghofer and Forget, 2012). Its presence has been observed through direct observations within fresh impact craters, exposed scarps, and excavations by the Phoenix lander (Byrne et al., 2009; Dundas et al., 2008, 2018; Mellon et al., 2008), and its widespread occurrence is indicated by gamma ray spectrometry, neutron fluxes, and radar data (Boynton et al., 2002; Feldman et al., 2002; Putzig et al., 2014). Further, ground-ice-related landforms, such as thermokarst terrain, patterned ground, and lobate crater ejecta morphologies constitute morphological evidence of the presence of subsurface ice on Mars (Costard and Kargel, 1995; Cull et al., 2010; Lefort et al., 2010; Mellon et al., 2008; Squyres and Carr, 1986).

Hale Crater is located on the north-eastern rim of the Argyre Basin in Mars' southern hemisphere (35°41′59.94"S, 36°24′0.07"W) and has a

* Corresponding author at: Université Savoie Mont Blanc, Laboratoire EDYTEM – UMR5204, Bâtiment « Pôle Montagne », 5 bd de la mer Caspienne, F-73376 Le Bourget du Lac cedex, France.
E-mail address: costanza.morino@gmail.com (C. Morino).

https://doi.org/10.1016/j.icarus.2022.115363
Received 7 July 2022; Received in revised form 23 October 2022; Accepted 15 November 2022
Available online 19 November 2022

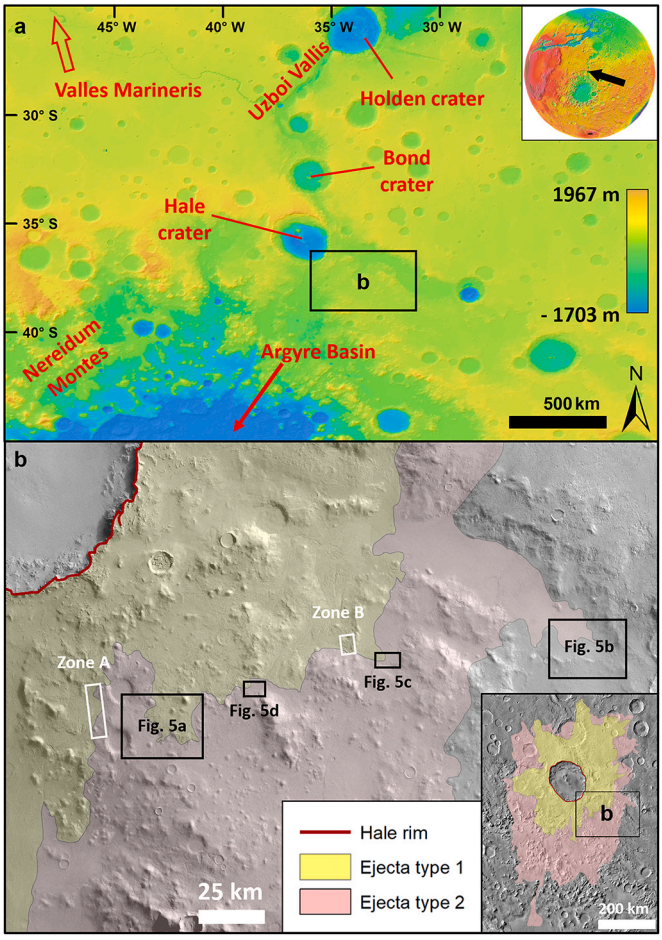

Fig. 1. Location of the study zone. a: Location of Hale crater on Mars. Inset map shows the location of the study area in panel b on a global view of Mars. Background is colourised and hillshaded relief from MOLA global mosaic (MOLA Science Team/Arizona State University); b: Study area located south-east of Hale Crater. Background is HRSC images H0489_000_nd4 and H0511_0000_nd4 (ESA/DLR/FU Berlin). White rectangles indicated as Zone A and Zone B are HiRISE image footprints (HiRISE credits: NASA/JPL/University of Arizona), black rectangles indicate the study areas with the locations of Fig. 5a-d. Inset map shows a simplified map of Ejecta type 1 and 2 of Hale crater, modified after Jones et al. (2011) on the THEMIS day-infrared global mosaic (NASA/JPL/ASU).

model age of 1 Ga (Early to Middle Amazonian; Hartmann, 2005; Jones et al., 2011). It is characterised by an elliptical shape and an asymmetrical expression of its central peak. Hale Crater is surrounded by lobate ejecta containing channels; its interior is filled with materials that are pervasively pitted, and numerous alluvial fans terminate on its floor. These landforms are thought to have been formed immediately after the impact and indicate an ice-rich composition of the target surface/subsurface (Barlow and Perez, 2003; El-Maarry et al., 2013; Jones et al., 2011; Tornabene et al., 2012).

Conical mounds are common in the south-eastern part of Hale Crater's ejecta flows (Collins-May et al., 2020) and are not found on any other parts of the ejecta, yet the precise origin of these mounds is unknown. Given the previously demonstrated role of ice in Hale's formation, this work aims to test if these conical mounds could form in analogous way to permafrost molards on Earth. Molards in permafrost terrains are conical mounds of debris on landslide deposits (Morino et al., 2019). They result from ice-consolidated blocks of debris that are generated and transported by landsliding, or a similar event that could result in the detachment of blocks of permafrost. The interstitial ice then thaws, and the debris consequently no longer forms a coherent block and collapses, forming a conical mound. Molards are described on Earth as rounded to pointy conical mounds that can be 0.3 to 12 m high, and up to 40 m in diameter (Milana, 2016; Morino et al., 2019; Sæmundsson et al., 2018). Their final morphology can vary depending on the initial ice content, the size and rheology of the material (reflecting the surrounding lithology), and the topographic and climatic context.

In this study, we test the hypothesis that the conical mounds in Hale crater are molards. We propose that they formed from the degradation of blocks of ice-cemented ground transported by the ejecta flows, suggesting that not all the ice was melted by the impact and that the ice itself was contained within the pores of the soil, rather than masses of glacial ice. In the following sections, we: i) present a regional geomorphological map of the south-eastern ejecta of Hale Crater; ii) analyse the spatial and topographic distribution of the Hale mounds at regional and local scales, and compare it to those of molards on the deposits of Mount Meager debris avalanche in Canada; and iii) compare the morphology and morphometrics of 2181 conical mounds at Hale Crater to those of terrestrial molards on the Paatuut and Niiortuut rock avalanches in Centralwest Greenland.

2. Geological settings

2.1. Hale Crater setting

The study area on Mars (36°30′8.95″-38°8′28.67"S, 35°28′24.51″-32°19′52.61"W) is located south-east of Hale Crater, an impact crater with an elliptical shape (125 km across, 150 km wide), which has a central peak and several wall terraces (Jones et al., 2011; Melosh, 1989). Its rim is elongated along the north-west – south-east axis, likely because the impactor came from the south-east heading towards the north-west (Schultz and Wrobel, 2012). This hypothesis is supported by the asymmetrical features of its central peak and ejecta blankets (Jones et al., 2011). In general, ejecta blankets are thicker and continuous near the original crater, and farther away become thinner and sparser (Melosh, 1989). Moreover, the size of debris particles decreases with the distance from the main crater (Melosh, 1989). Ejecta blanket morphology varies with the impactor velocity, the presence of an atmosphere and mostly with the target nature and ice content (Chapman, 2007).

Ejecta almost continuously covers the areas close to the rim of Hale Crater and was termed Type 1 ejecta by Jones et al. (2011). A more localised and discontinuous coverage of ejecta deposits characterises a wide region of Nereidum Montes, in which Hale Crater is located and was termed Type 2 (Fig. 1). The ejecta blankets show evidence of an ice-rich composition of the target surface, because they have lobate margins and are characterised by channels and polygonal patterns (Collins-May et al., 2020; Jones et al., 2011). It has been proposed that particularly large volumes of ground ice could have formed here because the Hale impact bisects Uzboi Valles (Fig. 1), which is thought to have transferred 150,000–450,000 m^3 s^{-1} of water between the Argyre Basin and the northern plains of Mars during the Late Noachian and Early Hesperian epochs (Grant and Parker, 2002; Grant and Wilson, 2018). Channels transported ejecta materials from Hale Crater, so are found within or originating from Hale's ejecta, radiating from Hale in all directions and reaching as far as 460 km from Hale's southwestern rim. Their highest concentration is south–southwest of Hale, on the northern slope of Argyre basin. They are up to a few kilometres across, flow downhill and around obstacles, are generally immature, and many are braided (Jones et al., 2011). Pre-existing channels and valleys funnelled Hale ejecta material too (Jones et al., 2011). Mounds are located within the Hale ejecta, and are sometimes characterised by angular boulders embedded at their tops and sides. Some also have craters or pits on their surfaces (Collins-May et al., 2020). There are also polygonally patterned surfaces comprising cracks and ridges forming sunken and raised rim polygons, respectively. Coalescing groups of sub-circular ponded and pitted material are found on the floor of and in the ejecta deposits of Hale crater (Jones et al., 2011). This pitted-ponded material is thought to indicate

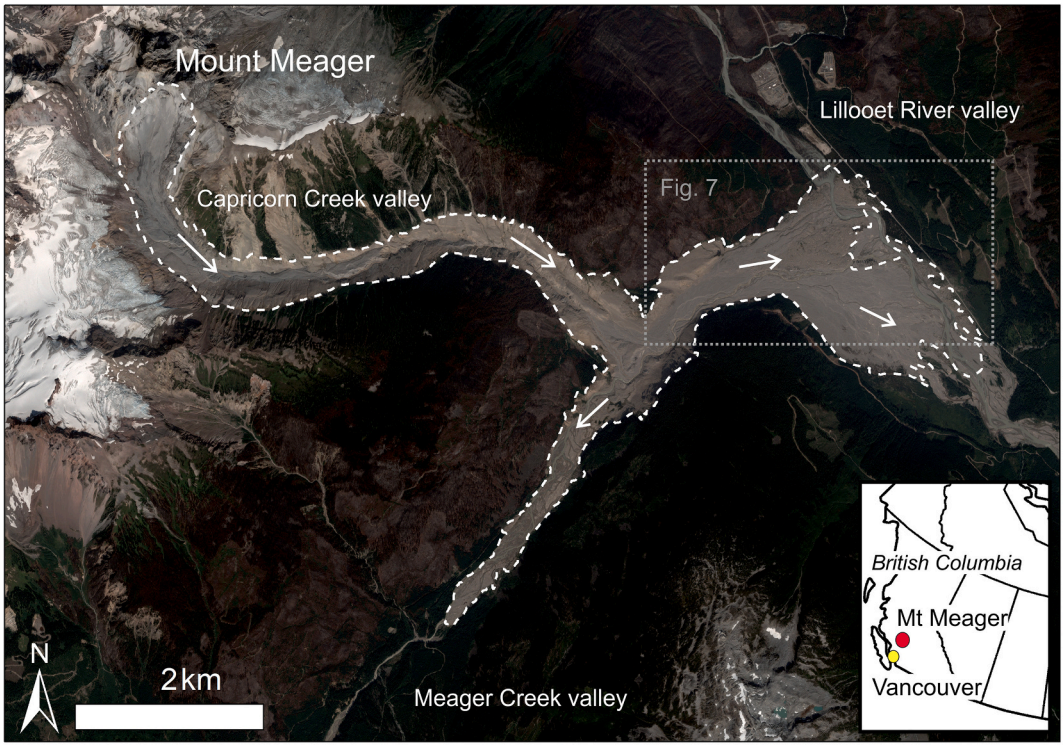

Fig. 2. Mount Meager area showing the boundary of the Mount Meager 2010 debris avalanche (dashed white line). Basemap Pléiades true colour satellite image from 2017 (DS_PHR1A_201508121923233_FR1_PX_W124N50_0718_02305, © Airbus Defence and Space 2015). Inset map shows the location of the study area in western Canada. White arrows show transport direction; the dotted grey rectangle shows the extent of Fig. 8 where the molards are located.

volatiles escaping from a mixture of impact melt and lithic clasts, forming suevite, i.e., impact-melt breccias (Bray et al., 2009; McEwen et al., 2007b; Mouginis-Mark et al., 2007; Tornabene et al., 2007).

2.2. Mount Meager setting

The Mount Meager volcano (50°37′22.8”N, 123°30′3.6”W, 2554 m a.s.l.) is a partially glacier-covered volcanic complex located in the southern Coast Mountains of southwest British Columbia, 150 km north of Vancouver and approximately 65 km northwest of the town of Pemberton (Fig. 2). It is part of the Mount Meager Volcanic Complex (MMVC), which consists of several coalesced stratovolcanoes ranging in age from Pliocene to Holocene, of which Mount Meager is the youngest (Read, 1978, 1990). Highly fractured, weak, and hydrothermally altered volcanic rocks, including pyroclastic rocks, lava flows, and rhyodacite domes, compose the volcanic complex (Read, 1978, 1990). The area was covered by the Cordilleran Ice Sheet during the last Pleistocene glaciation (Clague and Ward, 2011), and currently hosts numerous small alpine glaciers. Glacier erosion and retreat and consequent slope stress changes, the recent degradation of mountain permafrost, and the low strength of the fractured and altered volcanic rocks have all contributed to the gravitational instability of the area (Evans and Clague, 1994; Geertsema et al., 2006; Holm et al., 2004; Schwab et al., 2003). The area is one of the most prone to mass movements in Canada, being affected by prehistoric, historic and recent landslides (Friele et al., 2008; Friele and Clague, 2009).

The most recent landslide in MMVC occurred on 6 August 2010, mobilising about 50 $\times$ 10^6 m^3 of material (Guthrie et al., 2012; Roberti et al., 2018) (Fig. 2). The landslide was a channelised debris avalanche, in which a variety of deposits can coexist (Hungr et al., 2014; Iverson et al., 2015). It originated from the southern peak of Mount Meager, travelling for 13 km down the valleys of Capricorn and Meager creeks and into the Lillooet River valley (Allstadt, 2013; Guthrie et al., 2012; Moretti et al., 2015; Roberti et al., 2017). The debris avalanche was characterised by a complex and high mobility, as the failing mass divided during transport into a faster water-rich phase and a slower water-poor phase (Roberti et al., 2017). The debris avalanche might have been caused by elevated pore water pressures (Delcamp et al., 2016) caused by glacier melt and permafrost thaw at the end of the summer, a phenomenon already observed in other failures at Mount Meager (Bovis and Jakob, 2000; Holm et al., 2004; Mokievsky-Zubok, 1977). Tens to hundreds of molards characterise the landslide deposits; they are 1–8 m in height and 1 m^3 to ~2000 m^3 in volume (Roberti et al., 2017). Flow structures and spreading and extension along the flow direction suggest that the cones behaved as rigid portions of the landslide mass and came to rest before the surrounding material (Roberti et al., 2017). The Mount Meager debris avalanche represents a rare case of landslide where a fluid-dominated phase separated from a more solid-dominated phase. This characteristic, coupled with the presence of molards, makes the Mount Meager debris avalanche a good analogue-case for comparing its transport dynamics to those of the ejecta with mounds around Hale Crater on Mars.

2.3. Paatuut and Niiortuut settings

The Paatuut (70°15′33.53”N, 52°46′55.74”W) and Niiortuut (70°20′37.36”N, 53°10′54.80”W) rock avalanches are located in central west Greenland, on the south-western coast of the Nuussuaq Peninsula, facing the Vaigat Strait. The area is composed of the Palaeogene Vaigat and Maligât Formations, characterised by a series of hyaloclastite breccias and subaerial lava flows, that overlie Cretaceous-Palaeocene Atane and Danian Quikavsak Formations, formed of sandstones, mudstones and coal seams (Dam and Sønderholm, 1998; Pedersen and Pulvertaft, 1992). Despite the lack of active faulting in the Vaigat Strait (Voss et al., 2007), the setting of underlying prevalently unconsolidated sedimentary rocks overlaid by hard volcanic rocks is particularly prone to the generation of mass movements (Dahl-Jensen et al., 2004).

The south-western slope of Nuussuaq Peninsula is a landslide “hot

spot" in Greenland, hosting 67% of the post glacial landslides affecting the whole island (Svennevig, 2019), being favoured by slope deformations in response to glacial over-steepening (Pedersen et al., 2002). Permafrost degradation is thought to be one of the main causes for the occurrence of landslides in this area. The most recent is a frozen debris avalanche, described in a recent publication by Svennevig et al. (2022a), which occurred in June 2021 between the Niiortuut and the Paatuut rock avalanches, and whose deposits are characterised by molards. Svennevig et al. (2022a) hypothesised that the rock avalanche was conditioned, and possibly triggered by permafrost degradation in the talus slope in the source area.

The Paatuut rock avalanche occurred on 21 November 2000 at 1000–1400 m a.s.l. The 90 M m^3 mass was initially mobilised as a fall, evolved into a rock avalanche, entered the sea, and continued as a submarine slide, generating a tsunami (Dahl-Jensen et al., 2004; Pedersen et al., 2002). The trigger for the failure is thought to be repeated freeze and thaw cycles of water in surface cracks due to air temperature fluctuations in the days prior to the event (Dahl-Jensen et al., 2004). Extensive fields of molards are present on the rock-avalanche deposits (Benjamin et al., 2018), as well as longitudinal pressure ridges, whose occurrence has been linked in other landslides to the incorporation of ice into the flow (Huggel et al., 2005).

Very little was known about the December 1952 Niiortuut rock avalanche except for brief mentions of the events in the publications on the Paatuut rock avalanche (Dahl-Jensen et al., 2004; Pedersen et al., 2002). A recent publication by Svennevig et al. (2022b) recunstructs the dynamic of the event and attributes the failure onset to local permafrost degradation. The onshore area of the rock avalanche is 1.70 M m^2 and the rock avalanche deposits are covered by molards. The Niiortuut rock avalanche is a historical landslide that detached on the 15th of December 1952 around 14:00 local West-Greenland time near Niiortuut mountain in the Nuussuaq Peninsula. The rock avalanche mobilised several million cubic metres of deposits, resulting in a tsunami that hit the town of Qullissat 30 km away, causing minor damage to the town and one casualty.

3. Data and methods

3.1. Data for Hale Crater

Three data sets have been used to create the geomorphological maps at different scales of the study area in the south-east part of the Hale Crater ejecta. All data and images were downloaded from the PDS Geosciences Node Mars Orbital Data Explorer (ODE) and are listed in Supplementary Table 1. The regional map was made using data and images from the High Resolution Stereo Camera (HRSC, Mars Express; Neukum and Jaumann 2004). Two images with a spatial resolution of 25 m per pixel were used to cover the entire zone. The associated Digital Elevation Models (DEM) have a spatial resolution of 125–150 m per pixel. The HRSC images were used as a base for georeferencing 25 Context Camera images (CTX, Mars Reconnaissance Orbiter; Malin et al., 2007). These images allow a full coverage of the south-east part of the ejecta of Hale Crater with a spatial resolution of 6 m/pixel. While HRSC and CTX provide a complete coverage of the study area, only a few HiRISE images (High Resolution Imaging Experiment; McEwen et al., 2007a) at 25–50 cm/pixel are present in the zone, and only two have associated DEMs with a spatial resolution up to 1 m/pixel. These DEMs cover Zone A (37°29′16.31″-37°51′54.53"S, 35°48′30.18″-35°21′44.58"W) and Zone B (37°10′29.21″- 37°17′41.14"S – 33°23′18.98″-33°18′6.42"W), marked with white rectangles in Fig. 1. These are the two zones where morphometric measurements were made.

3.2. Data for Mount Meager

Oblique digital photos of the accumulation zone were collected one year after the occurrence of the landslide. A Canon EOS 30D with 28 mm lens, and a Canon EOS Digital Rebel XT and 50 mm were used from helicopter overflights at about 500 m elevation: 705 photos of the landslide were taken and used to generate three-dimensional models in Agisoft Photoscan (e.g., Fonstad et al., 2013; James and Robson, 2012; Westoby et al., 2012). Due to challenging field access, a field GPS campaign was not feasible; to georeference the model, control points were taken from 5 m resolution Geoeye-derived orthophoto and DEM. A high-resolution orthophoto (0.08 m/pixel ground resolution) and a DEM (0.34 m/pixel ground resolution) were extracted (Roberti et al., 2017).

3.3. Data for Paatuut and Niiortuut

In order to produce a DEM and orthophoto of the Paatuut and Niiortuut rock avalanche sample areas, oblique photogrammetry data were collected of the south-western slope of the Nuussuaq Peninsula in July–August of 2019. Images were acquired following the workflow described in Svennevig et al. (2015). The camera used was a handheld digital Single-Lens Reflex (SLR) Canon EOS-1Ds Mark III equipped with a calibrated Canon EF 35 mm f/1.4 L USM lens. The focal length of the lens was fixed to infinity to ensure that all photos were taken with the same focal length and that the whole scene is sharp. The photos were taken at a resolution of 21 megapixels (5616 × 3744) and stored in RAW format. The absolute position was recorded by an external GPS antenna and written into the image file directly giving an accuracy of +/− ~5 m. Images were recorded from a helicopter at cruise altitude of 50 to 300 m with 80–90% overlap. Using these photos, two different DEMs were produced at a spatial resolution of 15 cm/pixel, together with the associated orthophotos using the open source multiview photogrammetry software micmac (https://micmac.ensg.eu/). The ground control was taken from vertical aerial photographs taken in 1985 (5 m) combined with the 2 m/pixel ArcticDEM.

3.4. Regional geomorphological mapping of the south-east part of Hale Crater

Geomorphological units from Jones et al. (2011) were remapped using CTX images at a scale of 1:25,000 compared to 1:500,000 of the original map. We used a sinusoidal projection centred at −34°41′49.32"W, the centre longitude of the study zone and using the Mars2000 IAU datum.

All craters >60 m diameter were mapped in the area. These were used to examine the crater densities on the different units and to estimate the Hale ejecta thickness.

The estimation of the Hale ejecta thickness was made using craters that had fresh, sharp rims and that were filled with ejecta from the Hale impact, including craters superposing the ejecta and those covered by ejecta. Our aim was to use craters that were fresh when the Hale impact occurred and were then partly filled with the ejecta from Hale. For these craters we measured the crater diameters by firstly estimating the radii using the mean distance between the centre point of each crater and points extracted every 5 m along their rim. Diameters were then calculated by doubling the radii. The mean crater diameters were used to estimate the initial crater depth, calculated with Eq. 1 for a simple Martian crater (Garvin et al., 2003).

$$d = 0.21D^{0.81} \quad (1)$$

With: d: crater depth and D: crater diameter.

A mean elevation was calculated within a 25 m buffer around the centre point of each crater from the HRSC DEM. The mean elevation of the crater rim was also extracted from the DEM. The theoretical centroid elevations (calculated using equation Eq. 1) were compared to the measured centroid elevations. The estimated Hale ejecta thickness corresponds to the difference between these elevations.

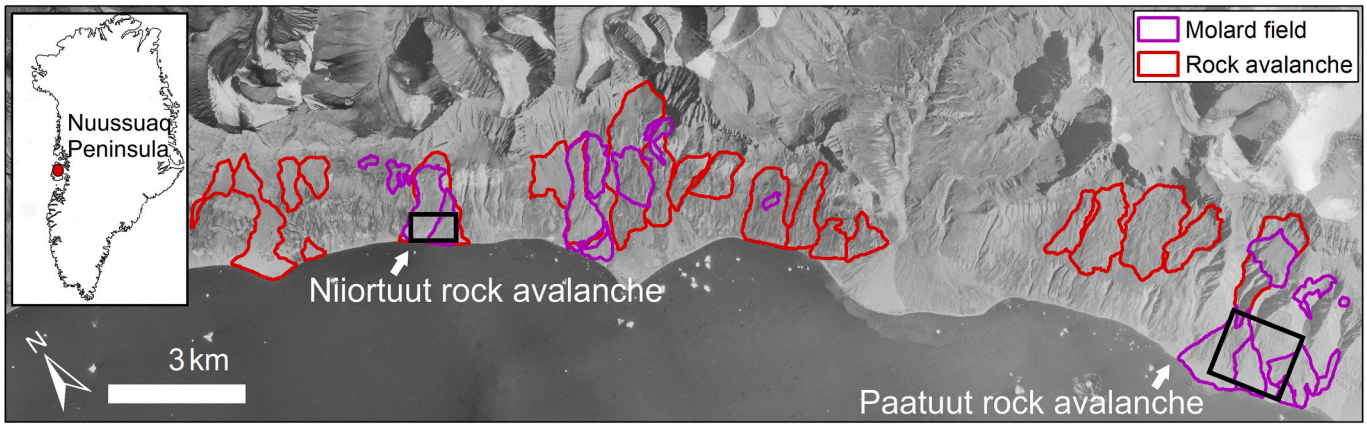

Fig. 3. The south-western slope of Nuussuaq Peninsula, showing the rock avalanches and molard field boundaries identified by field and airborne image observations. The black squares indicate the studied areas of Paatuut and Niiortuut rock avalanches. The basemap is vertical aerial photographs of the south coast of Nuussuaq Peninsula from 1985, available from SDFI (The Danish Agency for Data Supply and Infrastructure). Inset map shows the location of the study area within western Greenland.

3.5. *Morphometric analyses of the conical mounds*

We performed measurements of the morphometric characteristics of the conical mounds in Zones A and B of the Hale crater ejecta (Fig. 1). Measurements were made in a sinusoidal projection centred at −35°21′34.51"W for Zone A, and - 33°20'51.40"W for Zone B. Every mound visible at this scale was mapped as a polygon using 1 m contour lines generated from the HiRISE DEM, with the bottom contour line of

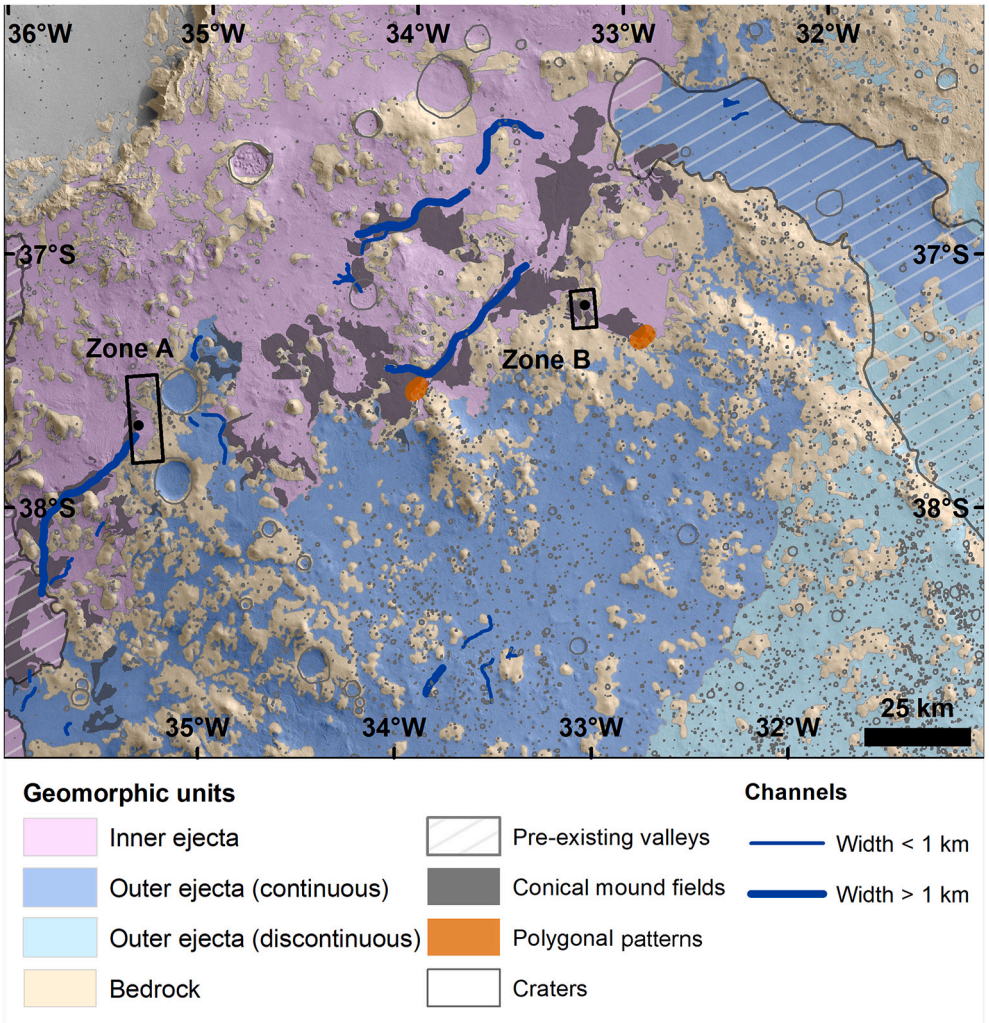

Fig. 4. Geomorphological map of the south-East area of Hale Crater. The area mapped is the same as for Fig. 1b. Polygonal patterns are buffered to 1500 m so they are visible at this scale. The black dots show the locations of Fig. 9a and b.

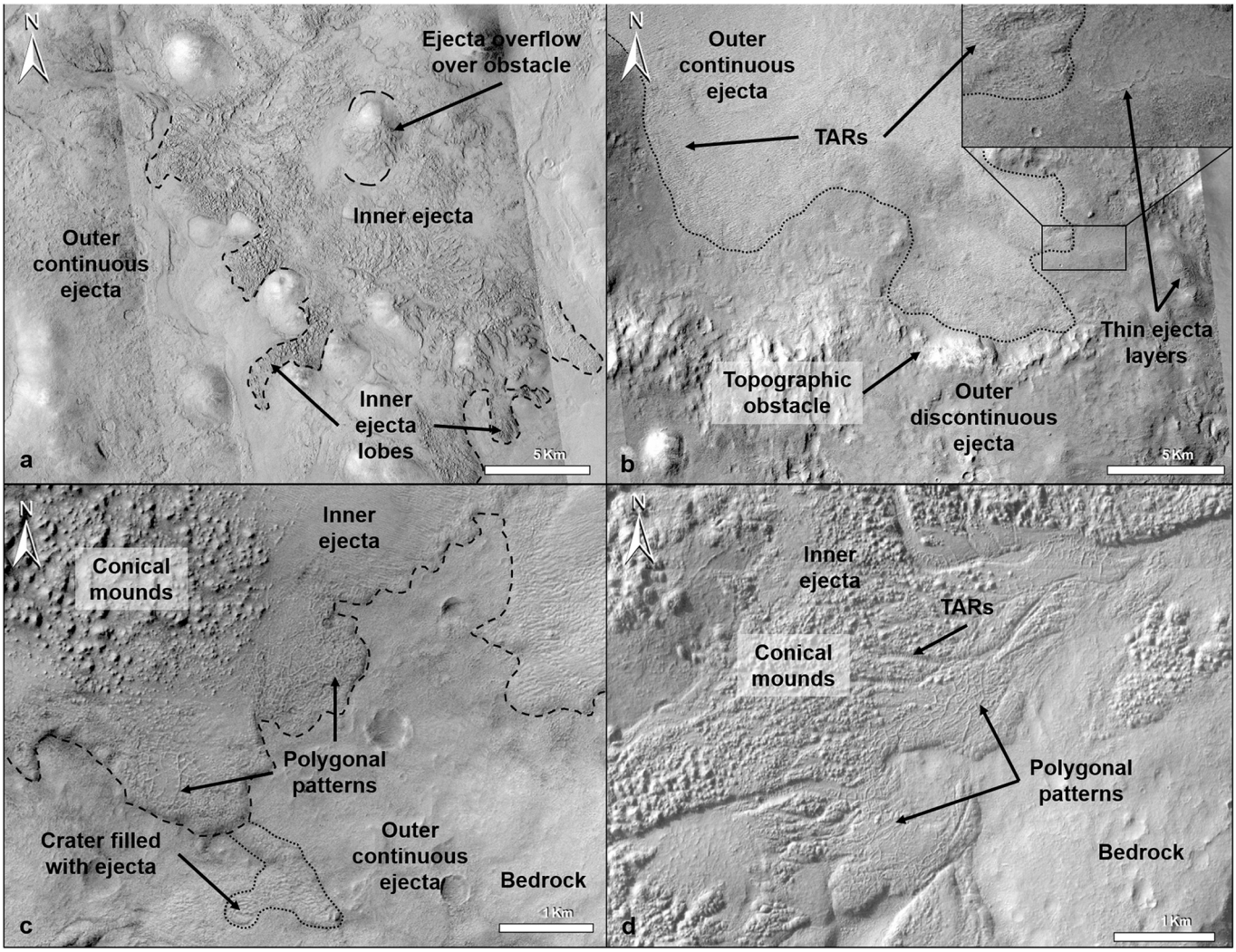

Fig. 5. a: Close-up (location visible in Fig. 1) of the boundary between the lobed Inner Ejecta and Outer Ejecta continuous Units. CTX images: B03_010896_1425_XI_37S034W, B10_013665_1423_XN_37S035W, B11_013731_1426_XN_37S035W; b: Close-up (location visible in Fig. 1) of the boundary between the Outer Ejecta continuous and Outer Ejecta discontinuous Units with the presence of TARs. CTX image: J04_046262_1434_XN_36S031W; c: Close-up (location visible in Fig. 1) of the association between conical mounds and polygonal patterns in the Inner Ejecta Unit. CTX image: G14_023858_1429_XI_37S033W; d: Close-up (location visible in Fig. 1) of the association between conical mounds, polygonal patterns and TARs in the Inner Ejecta Unit. CTX image: B01_010118_1433_XI_36S034W. CTX credits: NASA/JPL/MSSS.

the mound taken as the polygon outline. Conical mounds were measured if: i) their contours lines form ellipsoidal to circular closed lines and ii) loose blocks of rocks were observed either near or on their flank slopes.

The area, height, and flank slope angle of the isolated conical mounds were measured (Supplementary Fig. 1). Due to the gradual transition of these conical mounds into the surround terrain, a slight over- or underestimation of their area is possible. The area of the conical mounds was found by calculating the area of each mound's polygon (Supplementary Fig. 1). The heights of the cones were estimated from the difference between the highest and the lowest elevation points contained within the polygon for each mound (Supplementary Fig. 1). The slope map derived from the DEM was used to calculate the slope angle of the mounds. This was extracted along the line segment perpendicular to the long axis passing through the point of maximum elevation of each cone. A buffer of 50 cm was made around the maximum elevation point and these parts of the segments were removed, in order to eliminate the near-zero slope-values close to the summit. Then the clipped line segments were buffered by 1 m, and slopes were calculated using the mean value of the slope map derived from the DEM within these buffers.

For the morphometric measurements of the molards in the Paatuut and Niiortuut rock avalanches, we selected respectively 471 and 158 molards in a sample area of 0.6 km^2 and 0.4 km^2 (Fig. 3). The same method used for measuring the mounds on Hale was adopted, with every mound visible at 1:300 scale being mapped.

4. Results

4.1. Geomorphological features of Hale Crater south-east area

In the regional geomorphic map of the area south-east of the Hale Crater, we distinguished four geomorphological Units: "Type 1 to 3 Ejecta" and "Bedrock". These correspond to those used by Jones et al. (2011) ("Types 1 and 2 Ejecta" Units and "Bedrock"). For simplicity, we hereafter consider Types 2 and 3 as the "Outer Ejecta Unit", respectively "continuous" and "discontinuous", and Type 1 Ejecta Unit becomes the "Inner Ejecta Unit". This is because our ejecta thickness estimation (Fig. 6) based on crater diameter seems to show that Type 1 – Inner Ejecta is the thickest type of ejecta, whereas Type 2 – Outer Ejecta and 3 – Outer Ejecta have a similar thickness and geomorphological features.

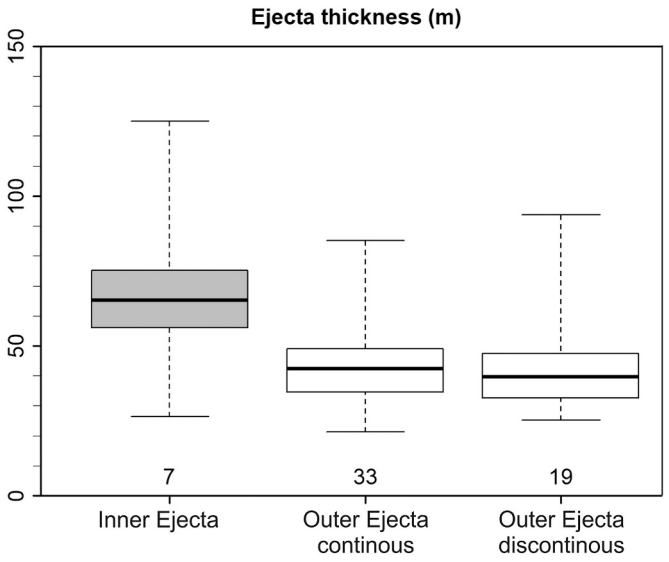

Fig. 6. Estimation of ejecta thickness for the Inner and Outer Ejecta Units. Number of craters is displayed beneath boxplots. For each boxplot, the thick horizontal black line represents the median, the box represents the interquartile range, and the whiskers represent the overall range. The crater diameter range is between 280 m and 2400 m.

The Type 3 - Outer Ejecta Unit can be considered as the discontinuous extension of Type 2 - Outer Ejecta Unit, showing the same ejecta blanket characteristics despite a difference in spatial coverage.

We also mapped the areas characterised by the presence of conical mounds, polygonal patterns, the main channels, and pre-existing valleys of the area (Fig. 5).

The Inner Ejecta Unit is the closest to the main crater and spreads in lobes up to 110 km from the crater rim towards the eastern ejecta boundary (Fig. 4). It seems to have flowed downhill and around obstacles in lobes, as it is visible on Fig. 5. Its surface can either appear rough (Fig. 5) or smooth, and is slightly cratered. Craters are mostly small (25 to 275 m and up to 1.5 km), where the bigger ones (>1.5 km) belong to the underlying geological unit, and are filled with ejecta. The thickness of the Inner Ejecta blanket is estimated to be around 65 m (Fig. 6; see Section 3.4 for the method). Almost all conical mounds are located in this Unit.

In its continuous sections the Outer Ejecta Unit is thinner than the Inner Ejecta Unit (around 45 m, Fig. 6) and spreads up to 200 km from the crater rim (Fig. 4). Its surface is smoother than Inner Ejecta Unit, but is more cratered and, as the Inner Ejecta Unit, hosts Transverse Aeolian Ridges (TARs; Balme et al., 2008; Chapman, 2007; Geissler and Wilgus, 2017; Zimbelman, 2010) in some locations (Fig. 5b).

The Outer Ejecta Unit transitions to discontinuous deposits 200 km from the main crater. In this region it appears either dusty and smooth or rocky and rough. Thin layers of ejecta deposits (estimated thickness is about 40 m; Fig. 6) can be observed, as in Fig. 5b, where ejecta seems to have flowed over an obstacle and was stopped by the topography.

The last geomorphological unit is "Bedrock" (Fig. 4). It is characterised by exposed rocky materials found at highest elevation zones throughout the study area, appearing rough nearer the main crater and smoother farther from it. The Unit shows clear discontinuous boundaries with ejecta units, which seem to have flowed around it.

Conical mound fields are present at the distal parts of the Inner Ejecta Unit, where the main channels are also found, and a few mounds are located inside these channels (Figs. 4, 5). These channels do not show evidence for erosion into the underlying terrain, but seem to be within the ejecta materials. The conical mounds range from 3 to 320 m in diameter, have pointy or rounded tops (Fig. 8), and they can be isolated or merged to form a succession of mounds. Conical mound fields are found in relatively low elevation areas, on surface slopes between 0° and 17°. Associated with the conical mounds are polygonal patterns and TARs. Polygonal patterns are at the distal boundaries of the conical mound fields at 37°20′39.67"S, 33° 1'15.13"W (Fig. 5c) and 37°31′12.00"S, 34° 4'47.99"O (Fig. 5d), and sometimes they intersect the mounds (Fig. 5c-5d). The polygons are 50 to 150 m in diameter. TARs can be found around and between conical mounds (Fig. 5d), and at the surface of Outer Ejecta Units, particularly at the boundaries of its more continuous part (Fig. 5b). Channels are linear to sinuous and have a lower relative elevation than the surrounding terrain (Fig. 4; depth up to 11–12 m, width 0.7–1.8 km). Their main orientation is roughly NE-SW. They can be isolated or joined-up to form small network. Two ~40 km wide pre-existing valleys filled with different ejecta types are located a) on the western side of the study area (having a N-S orientation), and b) on the north-eastern side of the study area (with a NW-SE orientation).

More than 7,185 craters greater than 275 m diameter can be found in the study area. They are circular to elliptic elevated rim structures that can be fully, partially or not filled with ejecta. The density of visible craters is less on the inner ejecta compared to the outer ejecta, specifically at the smallest diameters – this can be explained by the thicker inner ejecta having completely covered pre-existing smaller craters.

4.2. Distribution of conical mounds in Meager debris avalanche

To understand the distribution of conical mounds on the deposits of the Meager debris avalanche, we mapped the rheological phases observed in the field by Roberti et al. (2017) on the eastern side of the landslide deposits, and marked the perimeter of conical mounds from interpretation of the high-resolution (0.08 m/pixel) orthophoto and the shaded relief map from the 0.34 m/pixel DEM. In the Mount Meager debris avalanche, Roberti et al. (2017) were able to distinguish two main rheologies, a "Water-rich Phase" and a "Water-poor Phase". The water-poor phase produced up to 15-m thick deposits with numerous conical mounds and lobate boundaries (Fig. 7b-c). The water-rich phase formed flood-like deposits with no lithic debris and sparse tree trunks amid standing trees, which is particularly evident at the margin of the debris-avalanche deposits. The "Intermediate phase" is well represented in a terraced area, interpreted by Roberti et al. (2017) as an interaction zone between the other two main phases, being water-rich enough to run over the terrace and being water-poor enough to support hummocks and generate compressional structures.

The map in Fig. 7 shows the position of the conical mounds within the deposits left by each phase of the debris avalanche. The majority of the conical mounds (146 of 174 mounds) are concentrated in the deposits left by the water-poor phase (Fig. 7b-c). This zone had enough rheological strength to support the transfer and deposition of the blocks that formed the mounds. The area is characterised by ridges and shear zones (Fig. 7c) resulting from multiple generation of compressional, extensional, and transtensional movements (for more details see Roberti et al., 2017). Relatively few (14 for each phase) conical mounds are recognisable in the water-rich and intermediate phase.

4.3. Geomorphological and morphometric analyses of conical mounds

We analysed and measured the characteristics of conical mounds in Zone A and B (Fig. 8) in the SE ejecta of Hale Crater.

Fig. 10 shows height and area of the conical mounds represented in boxplots using a logarithmic scale on the y-axis. We have compared these measurements with those for molards in Paatuut and Niiortuut, which also have a circular to sub-circular planform and conical shape in cross-section (Figs. 9, 10).

Zone B cones are slightly taller than those of Zone A, but overall show similar height values (medians around 5–7 m), and their medians are one order of magnitude higher than those of molards in Niiortuut and Paatuut (Fig. 10), even though martian values are comparable to

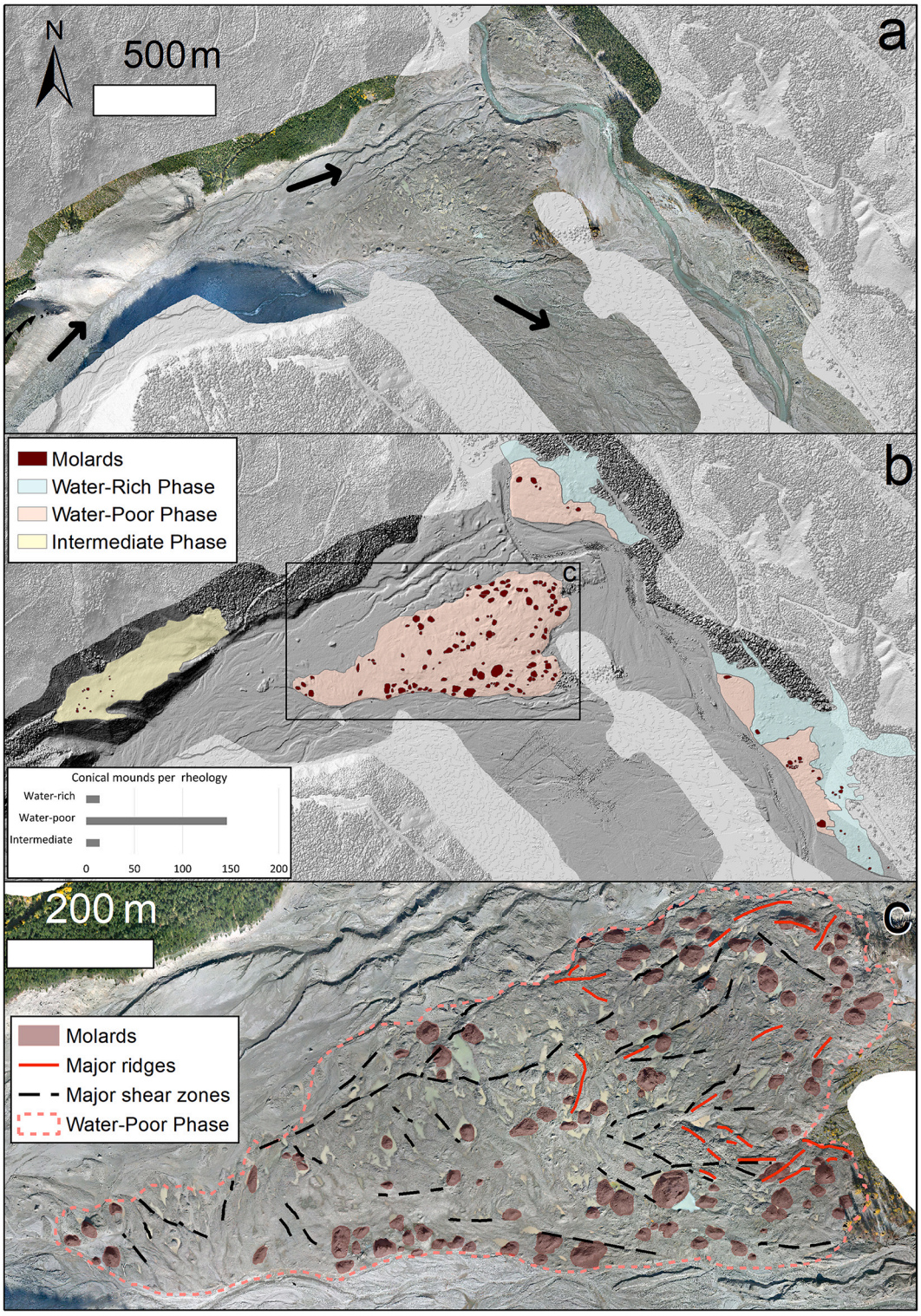

Fig. 7. a. Orthophoto of the eastern side of the Mount Meager debris avalanche deposits. Black arrows show the general transport direction. b. Map of the eastern side of the Mount Meager debris avalanche deposits and molards, overlaying the shaded relief of the 0.34 m/pixel DEM. The black box outlines the extent of panel c. In both a and b the base map layer is shaded relief of DEM at 1 m per pixel resolution. c. Map of the main structures (ridges and shear zones) of the water-poor phase of the eastern side of the Mount Meager debris avalanche.

terrestrial ones when looking at the maximum values of the terrestrial measurements. The mounds on Mars have larger areas than those on Earth: in both zones, Martian mounds have areas almost 2 orders of magnitude bigger than Niiortuut and Paatuut molards (Fig. 10). Flank slopes of cones in Zone B have higher values than those of Zone A, but have the same range of values of those of Niiortuut and Paatuut. In summary, martian conical mounds are taller and have a larger area than terrestrial molards, but are similarly steep.

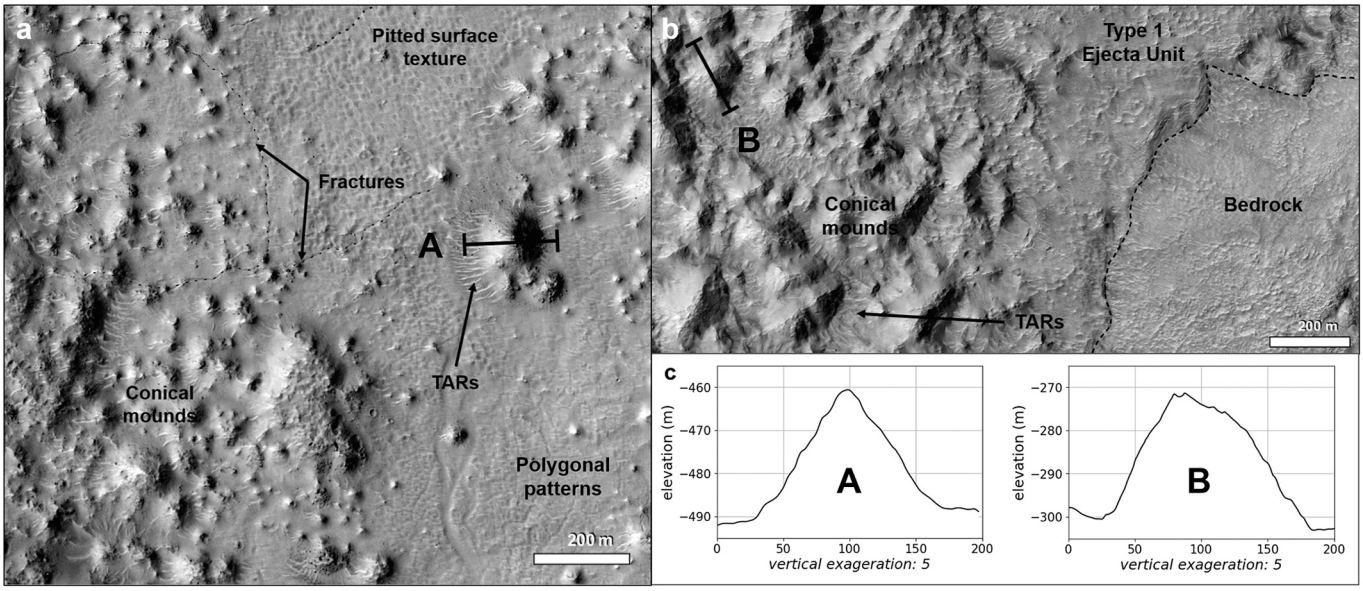

Fig. 8. Close up of conical mounds in Zone A and B. a –Conical mounds in Zone A, with pitted surface texture, polygonal patterns and fractures. The black line corresponds to the cross-section A of one of the conical mounds. HiRISE image ESP_013665_1420. b – Conical mounds in Zone B. The black line corresponds to the cross-section B of one of the conical mounds. HiRISE image ESP_057708_1425. HiRISE credits: NASA/JPL/UofA.

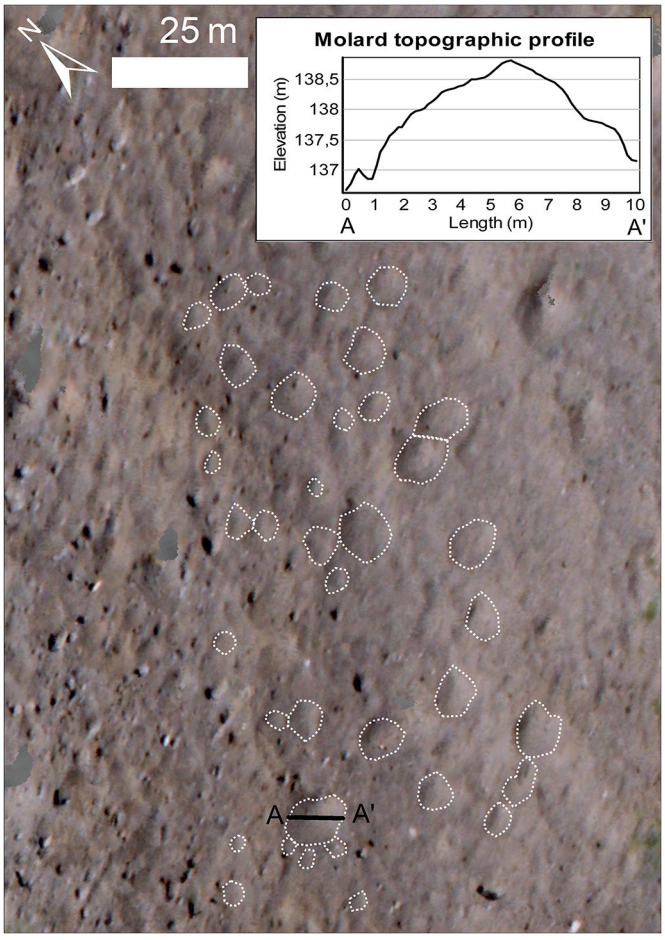

Fig. 9. Orthophoto at 0.15 cm/pixel resolution of part of the sample area in Niiortuut rock avalanche, Greenland, in which molards (white dashed outlines) have been measured. The topographic profile A-A' gives an example of the typical conical shape of the molards.

5. Discussion

5.1. Thickness and characterization of ejecta units and Meager debris avalanche

The Inner and Outer Ejecta Units show two different patterns of crater retention, where the inner ejecta lacks small craters as they have been entirely erased by the thicker ejecta here. Both ejecta units have lobate margins, and show evidence of fluidization, especially around obstacles (Figs. 4 and 5). This geomorphology has been described as characteristic of impact craters into volatile-rich target surface (Osinski, 2006; Senft and Stewart, 2008). During the impact, the presence of volatiles, i.e. water ice, in or on the target surface modifies the excavation processes and alter the speed and trajectory of projected and ground-hugging ejecta, which then spreads viscously. Since the Outer Ejecta Unit has spread further than the Inner one and is thinner, it can be interpreted as more fluid than the Inner Ejecta Unit and, therefore, has probably spread quicker than it.

The majority of mounds are concentrated on the surface of the Inner Ejecta Unit compared to the Outer Ejecta Unit. This also points towards the Inner Ejecta Unit being more fluid-poor, which is in agreement with the hypothesis of Collins-May et al. (2020). They suggest that the ejecta moved across the landscape with different liquified components, so that the coarser components separated from the fines of the flow through particle segregation and kinetic sieving (Johnson et al., 2012), leaving higher-standing mounds. The pristine state of the deposits is due to low erosion rates after the formation of Hale Crater (Grant and Wilson, 2018), similar to those that characterised other regions of Mars during the Amazonian (Farley et al., 2014; Golombek et al., 2006; Warner et al., 2010). The impact in Hale did not affect regional geomorphic activity or climate in the long term (Grant and Wilson, 2018), therefore the presence and morphology of the mounds is directly attributable to the emplacement of the ejecta.

We have observed a similar pattern on the deposits of Mount Meager debris avalanche in Canada, where molards are arranged along the distal parts of the fluid-poor terminal lobe of the depositional body. Almost all of the conical mounds are concentrated in the deposits left by the fluid-poor phase, whose rheological strength supported the transfer and deposition of the mounds. As discussed in Roberti et al. (2017), the areas where mounds are hosted are also characterised by deformation

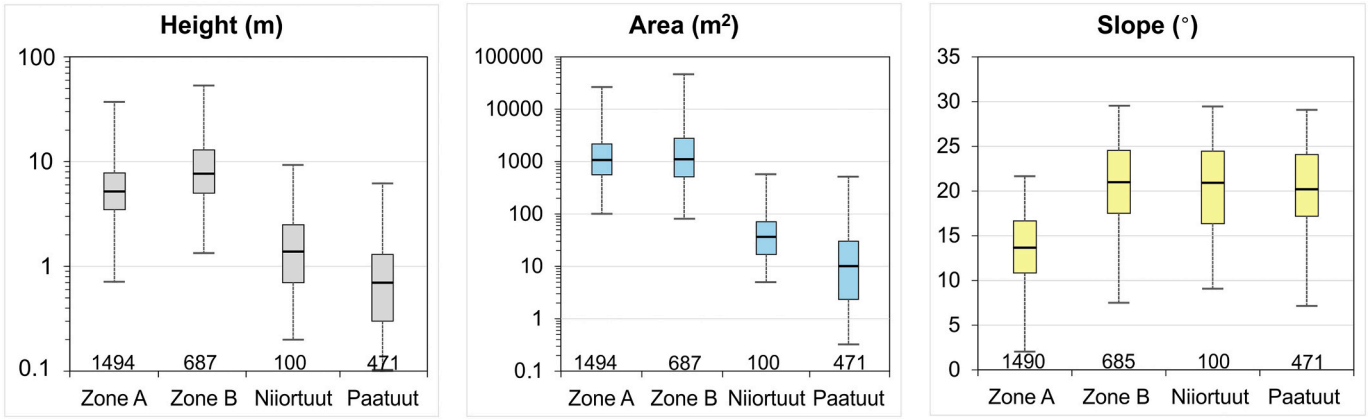

Fig. 10. Boxplots of the height, area, and flank slopes of the mounds in Zone A and Zone B of Hale Crater, Mars, and of molards in Niiortuut and Paatuut, Greenland; note that the vertical axes for height and area use a logarithmic scale. The whiskers show the maximum and minimum values, the boxes mark the interquartile range, and the thick horizontal black lines are the medians of each population. The numbers on the x-axis show the number of mounds in each population.

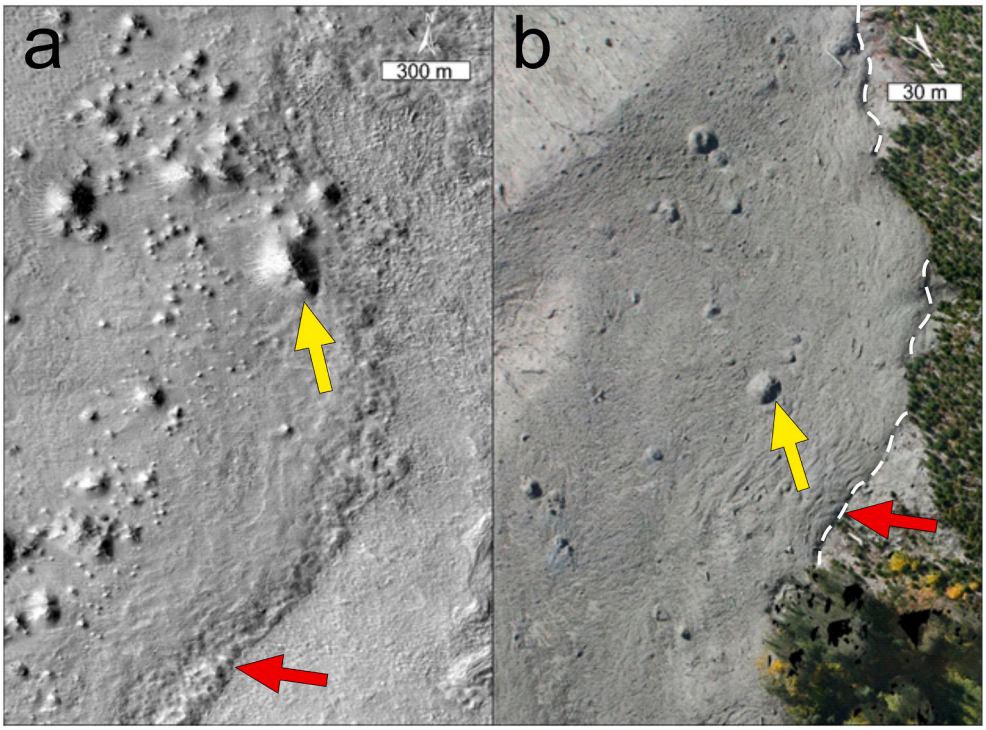

Fig. 11. a. View of the edge of one ejecta flow of the Inner Ejecta Unit with mounds on its surface (yellow arrow), Hale Crater, Mars. Ridges are visible towards the edge of the flow (red arrow). b. Orthophoto of the limit between a water-rich area (right of the dashed white line) and an intermediate-water-content area whose surface is scattered by molards (yellow arrow), Mount Meager, Earth. Ridges are visible at the contact between the two areas (red arrow).

structures such as ridges and lobes that accommodate compressional, extensional, and transtensional stresses of the water-poor phase of the avalanche (Fig. 7c, 11b). Similar ridges and fractures are observable at the edges of ejecta flows rich in molards in the Inner Ejecta Unit (Fig. 11a), which was sufficiently fluid-poor to support the transport of the mounds.

5.2. Characteristics and possible nature of conical mounds in comparison with terrestrial molards

Our measurements of both Hale Crater mounds and Greenlandic molards have been compared (Fig. 10). Martian cones are generally taller and larger in area than Niiortuut and Paatuut molards', yet the flank slopes are comparable. This size difference could have two explanations. The first is that the size difference is linked to the composition of the original ice-consolidated layer. If these martian conical mounds are molards, they were at first angular blocks of sediments consolidated by ground-ice. Morino et al. (2019) suggested that the initial ice content has a direct impact on the final molard height, flank slopes and summit morphology: high ice content blocks should form short, spread-out (i.e., small flank slope) and rounded molards. The estimated ice-content of Icelandic molards is about 15–20% of the initial block (Morino et al., 2019; Sæmundsson et al., 2018; Morino et al., 2021) and their heights range from few centimetres up to 10–12 m with flank slopes of 5–38°. Because the flank slopes do not substantially differ between Earth and Mars, the ice-content cannot explain the differences. The sediment granulometry should also have an impact on the molard morphology based on the particle angle of repose (Kleinhans et al.,

2011; Morino et al., 2019), but should only influence the flank slopes.

A second possible explanation of the size difference relates to differences in the initial frozen layer thickness. Morino et al. (2019) showed that the frozen layer thickness of the source material mobilised by a landslide has a direct impact on final molard size. Therefore, since the Inner Ejecta Unit is estimated to be between 60 and 70 m thick, it could transport larger initial blocks than either the Mount Meager debris avalanche or the Niiortuut and Paatuut avalanches, which had thinner deposits and less frozen source material.

In summary, Hale Crater's conical mounds are morphologically similar to terrestrial molards, but morphometrically different as they show higher values for almost every measured feature, except for flank slopes. This observation could be explained by a thicker initial frozen layer. On Earth, before degrading into molards, frozen blocks are transferred downslope by hundreds of metres to a few kilometres, so are subject to high energy during transport. In Hale, blocks experienced the maximum energy upon impact, but their subsequent transport occurred on low-gradient slopes, allowing the frozen blocks to be preserved during transport and to be degraded after coming to a rest position. Furthermore, the distribution of mounds in the most proximal part of the ejecta units indicates low-energy transport due to the less mobile, thicker and fluid-poor Inner Ejecta Unit.

The presence of martian conical mounds in Hale's ejecta has two important implications. First, that at least some of the ice involved in the impact was present as ice within the pores of the regolith and not as massive ice, thus providing the first constraints on the nature of the cryosphere at the time of the Hale impact. Second, the fact that ice-cemented sediment blocks were transported within the ejecta places important constraints on the nature/rheology of the flowing ejecta and its temperature. Although outside the scope of this work, these constraints could be used in hydrocode modelling to better understand the structure of the cryosphere.

Our geomorphological observations allow us to add more details to what happened after the impact in Hale. Ice-cemented blocks were projected by the impact, which were transported on the ejecta, particularly in its thicker and fluid-poor sections. During transport of the blocks, channels were active, and sometimes they contributed to the transport of the blocks, as some mounds are found in the channels too. These channels only show evidence of erosion into the ejecta materials. The surrounding pitted surfaces suggest loss of the volatiles from the ejecta materials, which is supported by the presence of fractures cross-cutting the conical mounds and polygonal patterns, which could represent desiccation (El Maarry et al., 2012). Some of the polygonal patterns could be due to thermal contraction while the materials were still ice cemented (Mangold, 2005). Ice-loss caused the blocks to degrade into conical mounds. TARs were formed from ejecta materials remobilised by the wind after volatile loss and successively deposited between the mounds.

6. Conclusions

The Hale Crater conical mounds are almost exclusively observed on the thickest part of the ejecta blanket, which is the closest to the main crater. This terrain shows landforms, such as polygonal patterns, lobate margins, internal channels, and pitted surface textures, suggesting the presence of a volatile during its emplacement and its subsequent loss.

Hale Crater mounds have similar flanks slopes to molards on Earth, and are generally taller with a larger area. The setting of the conical mounds within the lobate deposits of Hale Crater ejecta flows are consistent with that in the Mount Meager debris avalanche, where a fluid-poor phase supported the transport and deposition of blocks that formed conical mounds. We infer that Hale mounds result from blocks of ice-cemented ground that were thrown out in the impact and transported by the ejecta flows, which then degraded into cones of debris on loss of the interstitial ice. Comparison with terrestrial analogues reveals important geomorphological similarities between the ejecta flows of Hale and debris- and rock avalanches in periglacial environments on Earth, where substantial quantities of water derived by ground-ice are involved.

Both environmental characteristics and conical mound geomorphology seem to suggest that Hale Crater conical mounds could be the first Martian molards described, and that the volatile present in the target surface was in the form of ground-ice in the pores and not massive ice. Based on our observations, we suggest the following chronological history of Hale Crater ejecta and molard formation. About 1 Ga ago, Hale Crater was formed by the oblique impact of a projectile into an ice-rich target substratum. This impact induced several synchronous events: the formation of two types of ejecta blankets and the formation of ice-cemented-blocks projected by the impact. The two types of ejecta blankets were: a less mobile, thicker and fluid-poor Inner Ejecta Unit and a more mobile, thinner and fluid-rich Outer Ejecta Unit. Some of the bigger ice-cemented-blocks were incorporated in the Inner Ejecta Unit and were then transported in the flow of the ejecta to its distal end. Channels were simultaneously active and reworked some of the ejecta. Successively, loss of volatiles produced fractures and polygonal patterns and caused the degradation of volatile-rich blocks into molards. Finally, wind remobilised the fine component of the ejecta, forming TARs between the molards, at the distal boundary of the Inner Ejecta Unit and on the surface of the Outer Ejecta Unit.

Declaration of Competing Interest

None.

Data availability

Data will be made available on request.

Acknowledgements

This study is funded by the Agence Nationale de la Recherche in the framework of the project ANR-19-CE01-0010 PERMOLARDS.

SJC is grateful for financial support from the Programme National de Planétologie, and the French Space Agency CNES.

We acknowledge the financial support from Région Pays de la Loire, project étoiles montantes METAFLOWS (convention N° 2019-14294).

The project benefits from the dataset provided in the framework of IRSTEA DINAMIS - 2020-101-Sci-Pleiades and 2020-100-Sc. We thank DataTerra DINAMIS, the French Space Agency CNES and their ISIS programme for access to the Pléiades data.

Appendix A. Supplementary data

Supplementary data to this article can be found online at https://doi.org/10.1016/j.icarus.2022.115363.

References

Allstadt, K., 2013. Extracting source characteristics and dynamics of the August 2010 Mount Meager landslide from broadband seismograms. J. Geophys. Res. Earth Surf. 118, 1472–1490. https://doi.org/10.1002/JGRF.20110.

Balme, M., Berman, D.C., Bourke, M.C., Zimbelman, J.R., 2008. Transverse aeolian ridges (TARs) on Mars. Geomorphology 101, 703–720.

Barlow, N.G., Perez, C.B., 2003. Martian impact crater ejecta morphologies as indicators of the distribution of subsurface volatiles. J. Geophys. Res. Planets 108.

Benjamin, J., Rosser, N.J., Dunning, S.A., Hardy, R.J., Kelfoun, K., Szczuciński, W., 2018. Transferability of a calibrated numerical model of rock avalanche run-out: Application to 20 rock avalanches on the Nuussuaq Peninsula, West Greenland. Earth Surf. Process. Landf. https://doi.org/10.1002/esp.4469.

Bovis, M.J., Jakob, M., 2000. The July 29, 1998, debris flow and landslide dam at Capricorn Creek, Mount Meager Volcanic Complex, southern Coast Mountains, British Columbia. Can. J. Earth Sci. 37, 1321–1334.

Boynton, W.V., Feldman, W.C., Squyres, S.W., Prettyman, T.H., Brückner, J., Evans, L.G., Reedy, R.C., Starr, R., Arnold, J.R., Drake, D.M., 2002. Distribution of hydrogen in the near surface of Mars: evidence for subsurface ice deposits. Science (80-.) 297, 81–85.

Bray, V.J., Tornabene, L.L., McEwen, A.S., Mattson, S.S., 2009. Measurement of small-scale pits in the Corinto crater, Mars. In: 40th Annual Lunar and Planetary Science Conference, p. 1389.
Byrne, S., Dundas, C.M., Kennedy, M.R., Mellon, M.T., McEwen, A.S., Cull, S.C., Daubar, I.J., Shean, D.E., Seelos, K.D., Murchie, S.L., 2009. Distribution of mid-latitude ground ice on Mars from new impact craters. Science (80-.) 325, 1674–1676.
Carr, M.H., 2007. The Surface of Mars. Cambridge University Press.
Chapman, M., 2007. The Geology of Mars: Evidence from Earth-Based Analogs. Cambridge University Press.
Clague, J.J., Ward, B., 2011. Pleistocene glaciation of British Columbia. In: Ehlers, J., Gibbard, P.L., Hughes, P.D. (Eds.), Quaternary Glaciations - Extent and Chronology, Developments in Quaternary Sciences. Elsevier, pp. 563–573. https://doi.org/10.1016/B978-0-444-53447-7.00044-1.
Collins-May, J.L., Carr, J.R., Balme, M.R., Ross, N., Russell, A.J., Brough, S., Gallagher, C., 2020. Postimpact evolution of the Southern Hale Crater Ejecta, Mars. J. Geophys. Res. Planets 125 e2019JE006302.
Costard, F.M., Kargel, J.S., 1995. Outwash plains and thermokarst on Mars. Icarus 114, 93–112.
Cull, S., Arvidson, R.E., Mellon, M., Wiseman, S., Clark, R., Titus, T., Morris, R.V., McGuire, P., 2010. Seasonal H2O and CO2 ice cycles at the Mars Phoenix landing site: 1. Prelanding CRISM and HiRISE observations. J. Geophys. Res. Planets 115.
Dahl-Jensen, T., Larsen, L.M., Pedersen, S.A.S., Pedersen, J., Jepsen, H.F., Pedersen, G.K., Nielsen, T., Pedersen, A.K., Von Platen-Hallermund, F., Weng, W., 2004. Landslide and tsunami 21 November 2000 in Paatuut, West Greenland. Nat. Hazards 31, 277–287. https://doi.org/10.1023/B:NHAZ.0000020264.70048.95.
Dam, G., Sønderholm, M., 1998. Sedimentological Evolution of a Fault-Controlled Early Paleocene Incised-Valley System, Nuussuaq Basin, West Greenland.
Delcamp, A., Roberti, G., van Wyk de Vries, B., 2016. Water in volcanoes: evolution, storage and rapid release during landslides. Bull. Volcanol. 78, 1–12.
Dundas, C.M., Mellon, M.T., McEwen, A.S., Lefort, A., Keszthelyi, L.P., Thomas, N., 2008. HiRISE observations of fractured mounds: Possible Martian pingos. Geophys. Res. Lett. 35.
Dundas, C.M., Bramson, A.M., Ojha, L., Wray, J.J., Mellon, M.T., Byrne, S., McEwen, A. S., Putzig, N.E., Viola, D., Sutton, S., 2018. Exposed subsurface ice sheets in the Martian mid-latitudes. Science (80-.) 359, 199–201.
El Maarry, M.R., Kodikara, J., Wijessoriya, S., Markiewicz, W.J., Thomas, N., 2012. Desiccation mechanism for formation of giant polygons on earth and intermediate-sized polygons on Mars: results from a pre-fracture model. Earth Planet. Sci. Lett. 323, 19–26.
El-Maarry, M.R., Dohm, J.M., Michael, G., Thomas, N., Maruyama, S., 2013. Morphology and evolution of the ejecta of Hale crater in Argyre basin, Mars: results from high resolution mapping. Icarus 226, 905–922.
Evans, S.G., Clague, J.J., 1994. Recent climatic change and catastrophic geomorphic processes in mountain environments. Geomorphol. Nat. Haz. Elsevier 107–128.
Farley, K.A., Malespin, C., Mahaffy, P., Grotzinger, J.P., Vasconcelos, P.M., Milliken, R. E., Malin, M., Edgett, K.S., Pavlov, A.A., Hurowitz, J.A., 2014. In situ radiometric and exposure age dating of the Martian surface. Science (80-.) 343, 1247166.
Feldman, W.C., Boynton, W.V., Tokar, R.L., Prettyman, T.H., Gasnault, O., Squyres, S.W., Elphic, R.C., Lawrence, D.J., Lawson, S.L., Maurice, S., 2002. Global distribution of neutrons from Mars: Results from Mars Odyssey. Science (80-.) 297, 75–78.
Fonstad, M.A., Dietrich, J.T., Courville, B.C., Jensen, J.L., Carbonneau, P.E., 2013. Topographic structure from motion: a new development in photogrammetric measurement. Earth Surf. Process. Landf. 38, 421–430. https://doi.org/10.1002/esp.3366.
Friele, P.A., Clague, J.J., 2009. Paraglacial geomorphology of Quaternary volcanic landscapes in the southern Coast Mountains, British Columbia. Geol. Soc. London Spec. Publ. 320, 219–233.
Friele, P., Jakob, M., Clague, J., 2008. Hazard and risk from large landslides from mount meager volcano, British Columbia, Canada. Georisk 2, 48–64.
Garvin, J.B., Sakimoto, S.E.H., Frawley, J.J., 2003, January. Craters on Mars: Global geometric properties from gridded MOLA topography. In: Sixth International Conference on Mars.
Geertsema, M., Clague, J.J., Schwab, J.W., Evans, S.G., 2006. An overview of recent large catastrophic landslides in northern British Columbia, Canada. Eng. Geol. 83, 120–143.
Geissler, P.E., Wilgus, J.T., 2017. The morphology of transverse aeolian ridges on Mars. Aeolian Res. 26, 63–71.
Golombek, M.P., Grant, J.A., Crumpler, L.S., Greeley, R., Arvidson, R.E., Bell III, J.F., Weitz, C.M., Sullivan, R., Christensen, P.R., Soderblom, L.A., 2006. Erosion rates at the Mars Exploration Rover landing sites and long-term climate change on Mars. J. Geophys. Res. Planets 111.
Grant, J.A., Parker, T.J., 2002. Drainage evolution in the Margaritifer Sinus region. Mars. J. Geophys. Res. Planets 107, 1–4.
Grant, J.A., Wilson, S.A., 2018. The nature and emplacement of distal aqueous-rich ejecta deposits from Hale crater. Mars. Meteorit. Planet. Sci. 53, 839–856.
Guthrie, R.H., Friele, P., Allstadt, K., Roberts, N., Evans, S.G., Delaney, K.B., Roche, D., Clague, J.J., Jakob, M., 2012. The 6 August 2010 Mount Meager rock slide-debris flow, Coast Mountains, British Columbia: characteristics, dynamics, and implications for hazard and risk assessment. Nat. Hazards Earth Syst. Sci. 12, 1277–1294. https://doi.org/10.5194/nhess-12-1277-2012.
Hartmann, W.K., 2005. Martian cratering 8: Isochron refinement and the chronology of Mars. Icarus 174, 294–320.
Holm, K., Bovis, M., Jakob, M., 2004. The landslide response of alpine basins to post-little ice age glacial thinning and retreat in southwestern British Columbia. Geomorphology 57, 201–216.
Huggel, C., Zgraggen-Oswald, S., Haeberli, W., Kääb, A., Polkvoj, A., Galushkin, I., Evans, S.G., 2005. The 2002 rock/ice avalanche at Kolka/Karmadon, Russian Caucasus: assessment of extraordinary avalanche formation and mobility, and application of QuickBird satellite imagery. Nat. Hazards Earth Syst. Sci. 5, 173–187. https://doi.org/10.5194/nhess-5-173-2005.
Hungr, O., Leroueil, S., Picarelli, L., 2014. The Varnes classification of landslide types, an update. Landslides 11, 167–194.
Iverson, R.M., George, D.L., Allstadt, K., Reid, M.E., Collins, B.D., Vallance, J.W., Schilling, S.P., Godt, J.W., Cannon, C.M., Magirl, C.S., Baum, R.L., Coe, J.A., Schulz, W.H., Bower, J.B., 2015. Landslide mobility and hazards: implications of the 2014 Oso disaster. Earth Planet. Sci. Lett. 412, 197–208. https://doi.org/10.1016/j.epsl.2014.12.020.
James, M.R., Robson, S., 2012. Straightforward reconstruction of 3D surfaces and topography with a camera: Accuracy and geoscience application. J. Geophys. Res. Earth Surf. 117.
Johnson, C.G., Kokelaar, B.P., Iverson, R.M., Logan, M., LaHusen, R.G., Gray, J., 2012. Grain-size segregation and levee formation in geophysical mass lows. J. Geophys. Res. Earth Surf. 117.
Jones, A.P., McEwen, A.S., Tornabene, L.L., Baker, V.R., Melosh, H.J., Berman, D.C., 2011. A geomorphic analysis of Hale crater, Mars: the effects of impact into ice-rich crust. Icarus 211, 259–272.
Kleinhans, M.G., Markies, H., De Vet, S.J., Postema, F.N., 2011. Static and dynamic angles of repose in loose granular materials under reduced gravity. J. Geophys. Res. Planets 116.
Lefort, A., Russell, P.S., Thomas, N., 2010. Scalloped terrains in the Peneus and Amphitrites Paterae region of Mars as observed by HiRISE. Icarus 205, 259–268.
Malin, M.C., Bell, J.F., Cantor, B.A., Caplinger, M.A., Calvin, W.M., Clancy, R.T., Edgett, K.S., Edwards, L., Haberle, R.M., James, P.B., 2007. Context camera investigation on board the Mars Reconnaissance Orbiter. J. Geophys. Res. Planets 112.
Mangold, N., 2005. High latitude patterned grounds on Mars: Classification, distribution and climatic control. Icarus 174 (2), 336–359.
McEwen, A.S., Eliason, E.M., Bergstrom, J.W., Bridges, N.T., Hansen, C.J., Delamere, W. A., Grant, J.A., Gulick, V.C., Herkenhoff, K.E., Keszthelyi, L., 2007a. Mars reconnaissance orbiter's high resolution imaging science experiment (HiRISE). J. Geophys. Res. Planets 112.
McEwen, A.S., Hansen, C.J., Delamere, W.A., Eliason, E.M., Herkenhoff, K.E., Keszthelyi, L., Gulick, V.C., Kirk, R.L., Mellon, M.T., Grant, J.A., 2007b. A closer look at water-related geologic activity on Mars. Science (80-.) 317, 1706–1709.
Mellon, M.T., Arvidson, R.E., Marlow, J.J., Phillips, R.J., Asphaug, E., 2008. Periglacial landforms at the Phoenix landing site and the northern plains of Mars. J. Geophys. Res. Planets 113.
Melosh, H.J., 1989. Impact Cratering: A Geologic Process. New York Oxford Univ. Press, Oxford Clarendon Press.
Milana, J.P., 2016. Molards and their relation to landslides involving permafrost failure. Permafr. Periglac. Process. 27, 271–284. https://doi.org/10.1002/ppp.1878.
Mokievsky-Zubok, O., 1977. Glacier-caused slide near Pylon Peak, British Columbia. Can. J. Earth Sci. 14, 2657–2662.
Moretti, L., Allstadt, K., Mangeney, A., Capdeville, Y., Stutzmann, E., Bouchut, F., 2015. Numerical modeling of the mount meager landslide constrained by its force history derived from seismic data. J. Geophys. Res. Solid Earth 120, 2579–2599.
Morino, C., Conway, S.J., Balme, M.R., Helgason, J.K., Sæmundsson, Þ., Jordan, C., Hillier, J., Argles, T., 2021. The impact of ground-ice thaw on landslide geomorphology and dynamics: two case studies in northern Iceland. Landslides 18 (8), 2785–2812.
Morino, C., Conway, S.J., Sæmundsson, Þ., Kristinn Helgason, J., Hillier, J., Butcher, F.E. G., Balme, M.R., Jordan, C., Argles, T., 2019. Molards as an indicator of permafrost degradation and landslide processes. Earth Planet. Sci. Lett. 516 https://doi.org/10.1016/j.epsl.2019.03.040.
Mouginis-Mark, P.J., Tornabene, L.L., Boyce, J.M., McEwen, A.S., 2007. Impact melt and water release at tooting crater, Mars. In: Seventh International Conference on Mars, p. 3039.
Osinski, G.R., 2006. Effect of volatiles and target lithology on the generation and emplacement of impact crater fill and ejecta deposits on Mars. Meteorit. Planet. Sci. 41, 1571–1586.
Pedersen, G.K., Pulvertaft, T.C.R., 1992. The nonmarine Cretaceous of the West Greenland basin, onshore west Greenland. Cretac. Res. 13, 263–272.
Pedersen, S.A.S., Larsen, L.M., Dahl-Jensen, T., Jepsen, H.F., Pedersen, G.K., Nielsen, T., Pedersen, A.K., von Platen-Hallermund, F., Weng, W., 2002. Tsunami-generating rock fall and landslide on the south coast of Nuussuaq, central West Greenland. Geol. Greenl. Surv. Bull. 191, 73–93.
Putzig, N.E., Phillips, R.J., Campbell, B.A., Mellon, M.T., Holt, J.W., Brothers, T.C., 2014. SHARAD soundings and surface roughness at past, present, and proposed landing sites on Mars: reflections at Phoenix may be attributable to deep ground ice. J. Geophys. Res. Planets 119, 1936–1949.
Read, P.B., 1978. Geology, Meager Creek geothermal area, British Columbia.
Read, P.B., 1990. Mount Meager Complex, Garibaldi Belt, southwestern British Columbia. Geosci. Can. 17, 167–170.
Roberti, G., Friele, P., van de Vries, B.W., Ward, B., Clague, J.J., Perotti, L., Giardino, M., 2017. Rheological evolution of the mount meager 2010 debris avalanche, southwestern British Columbia. Geosphere 13, 369–390.
Roberti, G., Ward, B., van de Vries, B.W., Friele, P., Perotti, L., Clague, J.J., Giardino, M., 2018. Precursory slope distress prior to the 2010 Mount Meager landslide, British Columbia. Landslides 15, 637–647.
Sæmundsson, Þ., Morino, C., Helgason, J.K., Conway, S.J., Pétursson, H.G., 2018. The triggering factors of the Móafellshyrna debris slide in northern Iceland: intense

precipitation, earthquake activity and thawing of mountain permafrost. Sci. Total Environ. 621, 1163–1175. https://doi.org/10.1016/j.scitotenv.2017.10.111.
Schorghofer, N., Forget, F., 2012. History and anatomy of subsurface ice on Mars. Icarus 220, 1112–1120.
Schultz, P.H., Wrobel, K.E., 2012. The oblique impact Hale and its consequences on Mars. J. Geophys. Res, Planets, p. 117.
Schwab, J.W., Geertsema, M., Evans, S.G., 2003. Catastrophic rock avalanches, west-central BC, Canada. In: 3rd Canadian Conference on Geotechnique and Natural Hazards. Edmonton, AB, pp. 52–259.
Senft, L.E., Stewart, S.T., 2008. Impact crater formation in icy layered terrains on Mars. Meteorit. Planet. Sci. 43, 1993–2013.
Squyres, S.W., Carr, M.H., 1986. Geomorphic evidence for the distribution of ground ice on Mars. Science (80-.) 231, 249–252.
Svennevig, K., 2019. Preliminary landslide mapping in Greenland. Geol. Surv. Denmark Greenl. Bull. 43 https://doi.org/10.34194/GEUSB-201943-02-07.
Svennevig, K., Guarnieri, P., Stemmerik, L., 2015. From oblique photogrammetry to a 3D model–structural modeling of Kilen, eastern North Greenland. Comput. Geosci. 83, 120–126.
Svennevig, K., Hermanns, R.L., Keiding, M., Binder, D., Citterio, M., Dahl-Jensen, T., Mertl, S., Sørensen, E.V., Voss, P.H., 2022a. A frozen debris avalanche entraining warming permafrost ground - the June 2021 Assapaat landslide, West Greenland. Landslides 19, 2549–2567. https://doi.org/10.1007/s10346-022-01922-7.
Svennevig, K., Keiding, M., Korsgaard, N.J., Lucas, A., Owen, M., Poulsen, M.D., Morino, C., 2022b. Uncovering a 70-year-old permafrost degradation induced disaster in the Arctic, the 1952 Niiortuut landslide-tsunami in central West Greenland. Science of The Total Environment 160110.
Tornabene, L.L., McEwen, A.S., Osinski, G.R., Mouginis-Mark, P.J., Boyce, J.M., Williams, R.M.E., Wray, J.J., Grant, J.A., 2007. Impact melting and the role of subsurface volatiles: implications for the formation of valley networks and phyllosilicate-rich lithologies on early Mars. In: International Conf. on Mars VII. Lunar Planet. Sci. Inst. Contri.
Tornabene, L.L., Osinski, G.R., McEwen, A.S., Boyce, J.M., Bray, V.J., Caudill, C.M., Grant, J.A., Hamilton, C.W., Mattson, S., Mouginis-Mark, P.J., 2012. Widespread crater-related pitted materials on Mars: further evidence for the role of target volatiles during the impact process. Icarus 220, 348–368.
Voss, P., Poulsen, S.K., Simonsen, S.B., Gregersen, S., 2007. Seismic hazard assessment of Greenland. GEUS Bull. 13, 57–60.
Warner, N., Gupta, S., Lin, S., Kim, J., Muller, J., Morley, J., 2010. Late Noachian to Hesperian climate change on Mars: Evidence of episodic warming from transient crater lakes near Ares Vallis. J. Geophys. Res. Planets 115.
Westoby, M.J., Brasington, J., Glasser, N.F., Hambrey, M.J., Reynolds, J.M., 2012. "Structure-from-Motion" photogrammetry: a low-cost, effective tool for geoscience applications. Geomorphology 179, 300–314. https://doi.org/10.1016/j.geomorph.2012.08.021.
Zimbelman, J.R., 2010. Transverse aeolian ridges on Mars: first results from HiRISE images. Geomorphology 121, 22–29.